Detecting the slope movement after the 2018 Baige Landslides based on ground-based and space-borne radar observations

Yongsheng Li[a,*], Qisong Jiao[a], Xiuhong Hu[a], Zongliang Li[b], Bingquan Li[a], Jingfa Zhang[a], Wenliang Jiang[a], Yi Luo[a], Qiang Li[a], Renji Ba[b]

[a] Institute of Crustal Dynamics, China Earthquake Administration, Beijing, 100086, China
[b] ChengDu Center of China Geological Survey, Chengdu, 610081, China

ARTICLE INFO

ABSTRACT

On Oct. 11 and Nov. 3, 2018, two large-scale landslides occurred in the same location in Baige Village, Tibet, and massive rocks fell and encroached into the Jingsha River. These landslides posed a severe risk to the upstream and downstream areas. The occurrence, development and evolution of landslides are accompanied by a large number of changes in measurable variables. The deformation data are one of most important parameters for characterizing change and development trends of a landslide. This paper is centered on the results derived from ground-based radar and space-borne Synthetic Aperture Radar (SAR) images in the post-event phase to monitor the Baige landslides and to assess their residual risk. Two technologies play important roles in identifying and characterizing impending catastrophic slope failures: ground-based radar reveals the horizontal deformation, and satellite SAR images reveal the azimuth and range offset deformation. By combining satellite and ground-based SAR observations, we obtained high-precision three-dimensional (3D) deformation results and found that the vast majority of the instability regions mainly occur in the source area of the slope failures and that the direction of collapse converges from all sides to the middle. Additional information from UAV orthophoto maps and GNSS measurements also reveal that several cracks are distributed on the trailing edge of the landslide and are still moving. The comprehensive results revealed that the moving rock mass has still been remarkably active after the two landslide events. This study combined ground-based and space-borne SAR data to develop a long-term monitoring and stability evaluation process for implementation after a large landslide disaster. Based on the distribution characteristics of the 3D deformation fields, the present and future stability of the Baige Landslide was analyzed.

1. Introduction

Landslides are characterized by the downward movement of rocks and/or soils on slopes. Landslides can also be defined as slopes in an unstable state that may evolve into landslide hazards. The diversity of definitions reflects the complexity of landslides (Highland and Bobrowsky, 2008). The cause of landslides varies greatly and depends on factors such as slope, topography, soil type, basic geology and human activity. In late 2018 (Oct. 11 and Nov. 3, 2018), two large-scale landslides occurred successively in the same location in Baige Village, Boro Town, Tibet, China (Fig. 1). The entire rock mass of the slope slid rapidly and blocked the river, causing upstream inundation and downstream flooding. The Baige Landslide is located in the eastern part of the Qinghai-Tibet Plateau, which is in the northern part of the Hengduan Mountains regions. The Jinsha River valley zone between

the Mangkang Mountains and the Shaluli Mountains forms the high mountain canyon landform of the plateau. The downcutting erosion under rivers and gravity erosion are the main types of action in the process of slope evolution. According to the data from a regional geological survey, the Baige Landslide is located in the Jinsha River tectonic junction zone, which is mainly composed of tectonic melange. The Jinsha River junction zone is also an active tectonic zone, which is characterized by continuous uplift of the regional upper crust and active seismicity. Because of frequent geological activities, the structure of the mountain body is relatively fragmented and is easily affected by rainfall and earthquakes. The occurrence of a Baige landslide is a gravity-induced geological process of slope evolution in this area (Deng et al., 2019). Historical satellite optical data from 1966 to 2018 show that the landslide body in Baige has been sliding continuously over the past 50 years (Xu et al., 2018). During July 2017 and July 2018, the
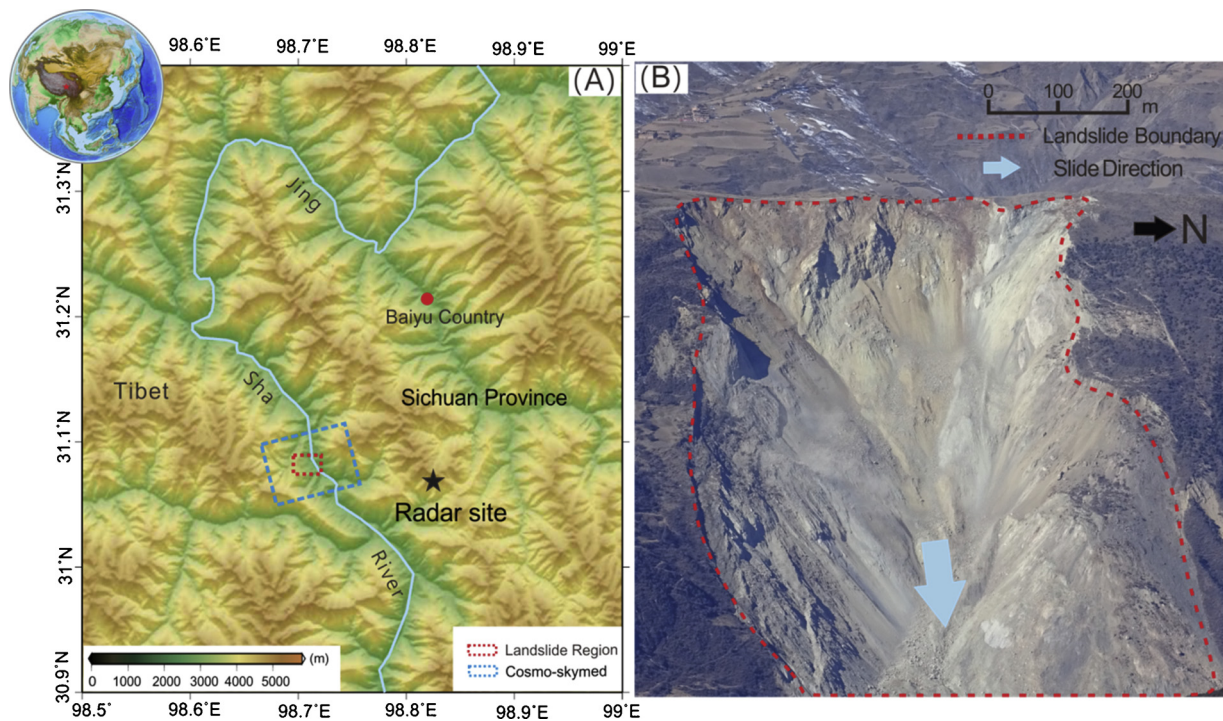

Fig. 1. Geographical setting and close-range photographs of the Baige Landslide. (A) Geographical location of the Baige Landslide. The blue box indicates the segments of ascending COSMO-SkyMed images. The red box represents the landslide region. The black star indicates the location of the ground-based radar. (B) Close-range photograph after the landslide taken on Dec. 4, 2018. The colour version of this figure is available only in the online version.

maximum displacement accumulation of the landslide body in the LOS direction was up to 25 m, as calculated by using SAR pixel offset tracking (Fan et al., 2019). Therefore, the collapse of the landslide was in accordance with expectations. Whether there will be another landslide or not requires further observations.

Landslide deformation data are among the most important parameters reflecting the process of landslide occurrence, development and evolution and are the necessary basic data for landslide monitoring and early warning (Casagli et al., 2010a). Space-borne interferometric synthetic aperture radar (InSAR) has achieved remarkable results in the research and application of landslide deformation monitoring (Corsini et al., 2006; Pierson and Lu, 2009; Calabro et al., 2010; Sun et al., 2015; Tong and Schmidt, 2016; Dai et al., 2016; Carlà et al., 2018; Hu et al., 2016, 2018). The advantages of space-borne InSAR systems are their wide spatial coverage and reliable monitoring accuracy. However, fixed orbit-related constraints, the long revisit time, insensitivity to deformation in the north-south direction and strict requirements for surface coverage types prevented the successful application of satellite InSAR in landslide emergency management (Bardi et al., 2014; Hu et al., 2016, 2018). The pixel-offset tracking (POT) method is also commonly used in landslide deformation monitoring (Wang and Jónsson, 2015, Wang et al., 2018a). The POT method solves two-dimensional deformation based on image intensity (azimuth and range direction of radar imaging). Unlike phase interferometry, POT can effectively extract large deformations with a resolution similar to or greater than the SAR resolution.

Compared with space-borne SAR systems, ground-based radar (GBR) systems can be deployed near the objects of interest to achieve continuous monitoring. GBR systems have been developed over more than a decade, and they mainly include the following two types: synthetic aperture radar (e.g. IBIS, FASTGBSAR) and real aperture radar (e.g. Gamma Portable Radar Interferometer, GPRI). The GBR is commonly used for applications in both natural disasters (Tarchi et al., 2003; Luzi et al., 2006, 2007; Herrera et al., 2009; Noferini et al., 2009; Casagli et al., 2010a, 2010b; Bozzano et al., 2011) and building safety

(Tapete et al., 2013; Serrano-Juan et al., 2016).

To study the deformation and stability of the sliding slope surface after the two Baige landslide events, several issues must be considered. How stable is the landslide? Will the landslide occur again? Where and how large will potential future landslides be? Answering these questions requires accurate mapping of the deformation patterns of landslides and information on how to avoid or mitigate the adverse impacts of landslides. From Dec. 4 to Dec. 10, 2018, the authors carried out a monitoring campaign using GBR equipment to accurately determine the location and magnitude of deformation and assess the stability of the sliding surface of the Baige Landslide. This paper will focus on analyzing the large slope failure using GBR and space-borne SAR images and providing technical support for subsequent landslide risk assessment.

2. Methodology

2.1. GBR equipment and data collection

The radar interferometry technique has been applied for surface deformation measurement for several years. In recent years, GBR platforms have become increasingly important because they can correct for inherent technical limitations in satellite SAR interferometry (e.g., limitations related to imaging cycle and observation direction). GBR can be used to obtain the maximum line of sight (LOS) signal according to the optimal measurement scheme. The ground-based interferometry radar system benefits from high temporal sampling, which is useful for reducing atmospheric phase delay errors and facilitating tracking of rapidly moving of landslides (Caduff et al., 2015, 2016). In this study, a GAMMA portable radar interferometer was employed. It can not only produce high spatial (~0.75 m in range, ~6.8 m in azimuth at 1 km) and temporal resolution maps of ground deformation, but can also be deployed flexibly to select the observation geometry (Caduff et al., 2015, 2016; Carlà et al., 2018). Although the design measurement range is 10 km, the equipment can scan to a maximum distance of 16.9 km in
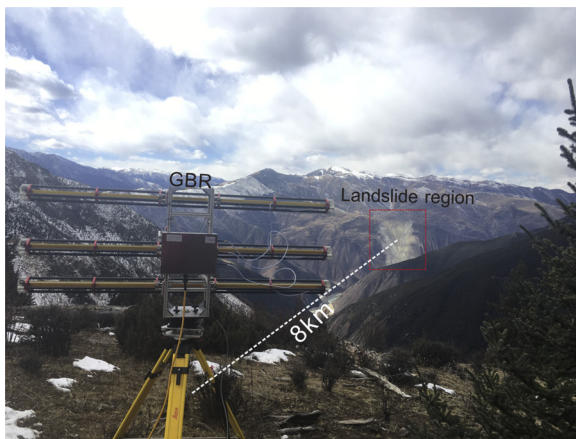
Fig. 2. Deployed GBR system and field of view of the landslide during the measurement campaign (photograph direction: west). The dotted rectangle is the location of the landslide.

certain campaigns (Xie et al., 2018). The capability of radar determines the critical phase gradient that can be obtained. The deformation between two adjacent spatial resolution units in the deformed field should be less than $\lambda/4$ (λ is the wavelength of the radar, which is 17.4 mm) to satisfy the requirement of phase unwrapping. Because ground imaging radar systems have a faster revisit time than satellite systems, the influence of time decorrelation can be greatly reduced.

To maximize the sensitivity of the GBR equipment in measuring deformation, the radar's observation vector must as parallel as possible to the displacement vector (Caduff et al., 2015). Due to the small elevation difference between the equipment and the landslide, the antenna incidence angle is set to 5 degrees below horizontal to maximize the sensitivity of the equipment to displacement. Considering the unobstructed observation field and the convenience of equipments assembly, the deployed position is approximately 8 km away from the landslide mass and has a field of view due west (Fig. 2). To encompass the full view of the landslide boundaries, we selected a 35° rotation angle and a 6.5 km to 9 km valid observation distance with respect to the equipment. The GBR equipment was deployed on Dec. 4, 2018. On the basis of Caduff's research (Caduff et al., 2015), we set the average time interval between scans to 10 min, which can recognize most of the deformation region without ambiguity and avoid most aliasing effects. The detailed imaging parameters of GBR are shown in Table S1 in the supporting information. A total of 775 scenes were collected in this monitoring campaign.

2.2. Atmospheric error correction of GBR

The GBR operates at a radar frequency of 17.2 GHz (Ku band), which is sensitive to micro-change of deformation in ground objects. The high radar frequencies show a high sensitivity to atmospheric phase delay (Zebker et al., 1997). Therefore, the additional phase contribution due to the difference in atmosphere conditions such as temperature and humidity cannot be neglected.

Typically, a linear phase ramp is mixed in the GBR interferograms, which is likely dependent on the propagation distance of the microwave during a scanning survey (Wang et al., 2018b). The most commonly used method is to simulate a distance-dependent linear phase ramp and then subtract it from the original interferogram (Lowry et al., 2013). However, in steep mountainous terrain, height-dependent atmospheric effects can cause strong perturbations, which act as the turbulent atmospheric phase presented in the GBR interferogram (Caduff et al., 2015; Monserrat et al., 2014). The Baige Landslide is located in an area with steep topography, and the water vapor environment changes continuously even over the course of a few minutes. The severely

turbulent atmosphere will superimpose a nuisance signal on the displacement phase and reduce the accuracy of estimated displacements. All of these issues have posed great challenges to this measurments.

This study adopted a spatial filtering method with a large filter window for estimating atmospheric path delays. However, the difference between the original deformation signal and the atmospheric signal is very large, and filtering interferograms directly will weaken the intensity of deformation signals and decrease the magnitude of the deformation results. This work benefits from a sufficient number of independent observations, and averaging these observations contributes to significantly reducing the phase component related to the turbulent atmosphere (Rouyet et al., 2017). The average results represent the deformation rate throughout the observation period. The deformation component is reassigned to each unwrapped interferogram; then, this component is subtracted from the original unwrapped phase. The residual phase is mainly composed of the nonlinear deformation and atmospheric phase. The residual phase is filtered to mitigate the atmospheric phase error and then to retrieve the nonlinear deformation signals for each interferogram.

2.3. GBR InSAR time series analysis

The GBR interferometric processing strategy is much simpler than that of space-borne data. Because of the zero-spatial baseline, the GBR does not require terrain removal or orbit error corrections. In the temporal dimension, the interferogram coherence is guaranteed to a large extent because of short time interval of the observation. Based on the ideas of the space-borne SAR interferometric time series analysis method, this paper constructs a ground-based SAR radar time series deformation algorithm to retrieve the temporal behavior of the landslide body.

(1) All small baseline interferometric pairs are processed. Starting from the single look complex (SLC) image set, interferometric pairs are generated according to the appropriate registration strategy. We created a temporal network of interferograms based on the criterion similar to that of the SBAS algorithm: the adjacent four scenes before and after each SLC acquisition in time (Berardino et al., 2002; Lowry et al., 2013), and 2250 interferograms were generated. The interferograms were subjected to 5×5 multilook processing and analyzed using an adaptive filter (Goldstein and Werner, 1998), and a minimum-cost flow algorithm was employed to unwrap the phase with coherence higher than 0.7 (Chen and Zebker, 2002). Then, the unwrapped interferograms and intensity images were converted into a Cartesian coordinate system with a resolution of 5 m.

(2) High coherence regions were identified based on GBR unwrapped interferograms and the coherence map. We evaluated interferometric temporal coherence to identify high-coherence regions and mask the low-coherence areas of the unwrapped phase.

(3) All masked unwrapped interferograms were stacked. The stacking procedure may reduce obvious phase shifts caused by atmosphere turbulence.

(4) The deformation accumulation was allocated to each interferogram, and the reassigned deformation phase was then subtracted from each original unwrapped interferogram.

(5) The residual phase mainly included atmospheric phase screen error and nonlinear deformation components. The residual phase was filtered to mitigate the atmospheric phase error and then the retrieved nonlinear deformation signal was processed for each interferogram. The details are described in Section 2.2.

(6) A singular value decomposition (SVD) inversion was carried out to obtain the nonlinear deformation rate. The nonlinear rate values were added back to the mean velocity fields and then accumulating them. We used a locally weighted linear regression filter with a filter window size of ˜0.1 days (144 min, 15 epochs) to smooth the displacement time series (Handwerger et al., 2019). Lastly,

temporal deformation evolution was determined.

2.4. Three-dimensional inversion

POT uses image cross-correlation technology to track the change of the target position in the SAR amplitude and can provide unambiguous ground displacement measurements to monitor large deformed regions. The cross-correlation quality is a determining factor used for evaluating the accuracy of pixel-offset measurements, which is one order of magnitude lower than that of InSAR and approximately one-tenth to one-twentieth the size of the SAR image resolution unit (Wang and Jónsson, 2015, 2018a). POT does not have cycle ambiguity, and even under the condition of InSAR decorrelation, it can obtain two-dimensional deformation fields from several meters to tens of meters. Although the accuracy of offset tracking analysis is lower than that of InSAR technology, this method has incomparable advantages in monitoring strong deformation fields, such as coseismic and landslide areas (Fielding et al., 2013; Raucoules et al., 2013; Himematsu and Furuya, 2016). In addition, the method can extract the deformation field of both the azimuth and range directions so that the north-south direction of the deformation can be obtained by the azimuth displacement field.

Space-borne and ground-based instruments have different imaging geometries, making interpretation of deformation challenging, especially if the deformation is spatially complex. This paper will combine two different sources from GBR and POT for inverting the measurements of east/north/up (ENU) deformation (3D deformation)

According to the geometric relationship between POT measurement and 3D deformation, we assume that when the target is far from the radar, the range direction deformation d_r is positive; in contrast, approaching the radar, the d_r is negative. Assuming d_{az} is positive when the deformation is along the azimuth direction, d_{az} and d_r can be represented by three components of ENU deformation (d_U d_N d_E).

$$d_r = d_U \cos\theta - \sin\theta[d_N \cos(\alpha - 3\pi/2) + d_E \sin(\alpha - 3\pi/2)]$$
$$d_{az} = d_U 0 + d_N \sin(\alpha - 3\pi/2) - d_E \cos(\alpha - 3\pi/2) \tag{1}$$

where θ indicates the angle of incidence of a satellite and α indicates the angle between direction of satellite flight (heading angle) and north direction(clockwise).

For GBR, assuming that the incidence angle of the radar is θ_G, the angle between the horizontal projection of the radar LOS and the north direction is α_G. Then, the LOS deformation of the GBR can be decomposed into

$$d_G = d_u \cos\theta_G - d_N \sin\theta_G \cos\alpha_G + d_E \sin\theta_G\sin\alpha_G \tag{2}$$

By combining the results of offset tracking and GB InSAR, we construct the following formula:

$$\begin{pmatrix} d_r \\ d_{az} \\ d_G \end{pmatrix} = \begin{pmatrix} \cos\theta & -\sin\theta\cos(\alpha - 3\pi/2) & -\sin\theta\sin(\alpha - 3\pi/2) \\ 0 & \sin(\alpha - 3\pi/2) & -\cos(\alpha - 3\pi/2) \\ \cos\theta_G & \sin\theta_G\cos\alpha_G & \sin\theta_G\sin\alpha_G \end{pmatrix} \cdot \begin{pmatrix} d_U \\ d_N \\ d_E \end{pmatrix} \tag{3}$$

The least-squares (LS) method is then used to solve for the 3D deformation.

3. Results and analyses

3.1. GBR results

The deformation results of GBR are obtained by using the algorithm described in Section 2. We investigate how the deformation is distributed spatially and evolves over time. Fig. 3 shows that the deformation is mainly concentrated on the right side of the viewing angle and centered on the landslide body. The corresponding animation of the deformation accumulating along the GBR LOS from Dec. 4 to Dec. 10, 2018 is presented in Video S1in the supporting information.

The landslide is inaccessible because of the dangerous conditions. Artificial corner reflectors cannot be successfully placed on the landslide surface. Thus, GBR image geocoding is a challenge in this complicated geographic environment. There are two steps to solve this problem.

(1) According to the position coordinates, the azimuth initial, start and end scanning angles and measuring distance, position of the interferogram are preliminarily determined. First, the zero-degree azimuth of the radar is determined according to the initial azimuth angle and position of the radar. Then, the scanning range of the radar is determined based on the azimuth start and end angles. Finally, the radar imaging region is determined according to the near range and the far range. See the position of the blue sector box in Fig. 4.

(2) On the basis of the preliminary correction, displacement maps were manually geocoded accurately using photogrammetric results and a high-resolution Digital Surface Model (DSM) derived from unmanned aerial vehicle (UAV) images collected on Dec. 6, 2018.

The geocoded deformation rate results are superimposed on the satellite optical image and the UAV-derived DSM in Figs. 4 and 5, and the 3D view of the deformation rate map is presented in Fig. S1 in the supporting information.

Fig. 5 shows the enlarged stacking results in terms of the mean displacement rate. The red dotted line represents the clearly identifiable boundary of the landslide body. Fig. 5(A) shows that the main deformation is distributed along the upper part of the sliding bed. A maximum LOS displacement rate of ˜230 mm/day was observed during the 6-day survey period. There are many decorrelation areas caused by the rapid motion of sandy soil and the absence of rock outcrops Fig. 5(B) shows that the maximum inversion residual value is approximately -3 mm/day. The debris of the landslide accumulates and falls continuously, which results in the uncertainty of the deformation characteristics.

After the landslide event on Oct. 11, 2018, 16 real-time GNSS landslide monitoring devices were deployed at the trailing edge of the landslide (Fan et al., 2019). Some devices were damaged due to the collapse of the unstable slope in the second event on Nov. 3, 2018. At least six GNSS devices are still working. We selected three available GNSS devices (G1, G2 and G3 in Fig. 5A) with obvious deformation signals to verify the accuracy of the results of the GBR. Because the LOS direction of the GBR is nearly horizontal, we projected the GNSS horizontal deformation results with 1 -h sampling interval to the LOS-parallel direction to compare the consistency between the results of GBR and GNSS (Fig. 6). Fig. 6A and B represent points G1 and G2, respectively, in Fig. 5, which are located on the left trailing edge of the landslide. Fig. 6C represents point G3, which is located on the right edge. For GNSS, the deformation signal exhibits obvious periodic variation, which may be caused by the multi-path effects (Atkins and Ziebart, 2016). For GBR, the deformation evolution results are much smoother because we used a linear regression filter in the time series analysis stage. Comparing the results of GNSS and GBR, we can determine that the deformation trends of the two measurements maintain high consistency.

We selected six representative points (P1-P6) for the locations of the largest local deformation rates in Fig. 5(A) and analyzed the deformation characteristics of these points over time in Fig. 7. All the deformation characteristics are coincident, and the maximum cumulative deformation of point 1 is approximately 1400 mm. This point is located at the left trailing edge of the landslide mass (looking toward the sliding direction). The deformation rates of point 2, point 5 and point 6 remained relatively stable during the period from Dec. 5 to Dec. 9, 2018, while the rates of point 1, point 3 and point 4 increased slightly, mainly due to the disintegration of fractured bedrock (Deng et al., 2019). However, from Dec. 9 to Dec. 10 the overall deformation rate of several
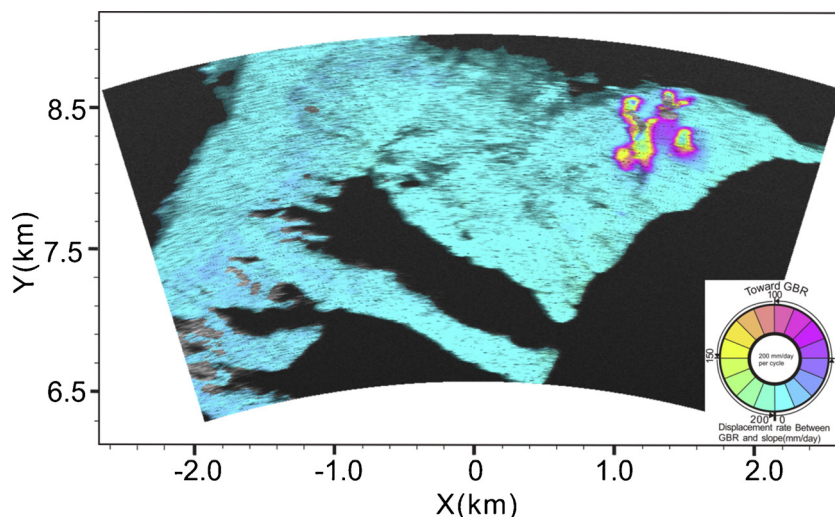
Fig. 3. LOS mean deformation velocity map produced by the ground-based radar relative to the period of Dec. 4 to Dec. 10, 2018. The colour version of this figure is available only in the online version.
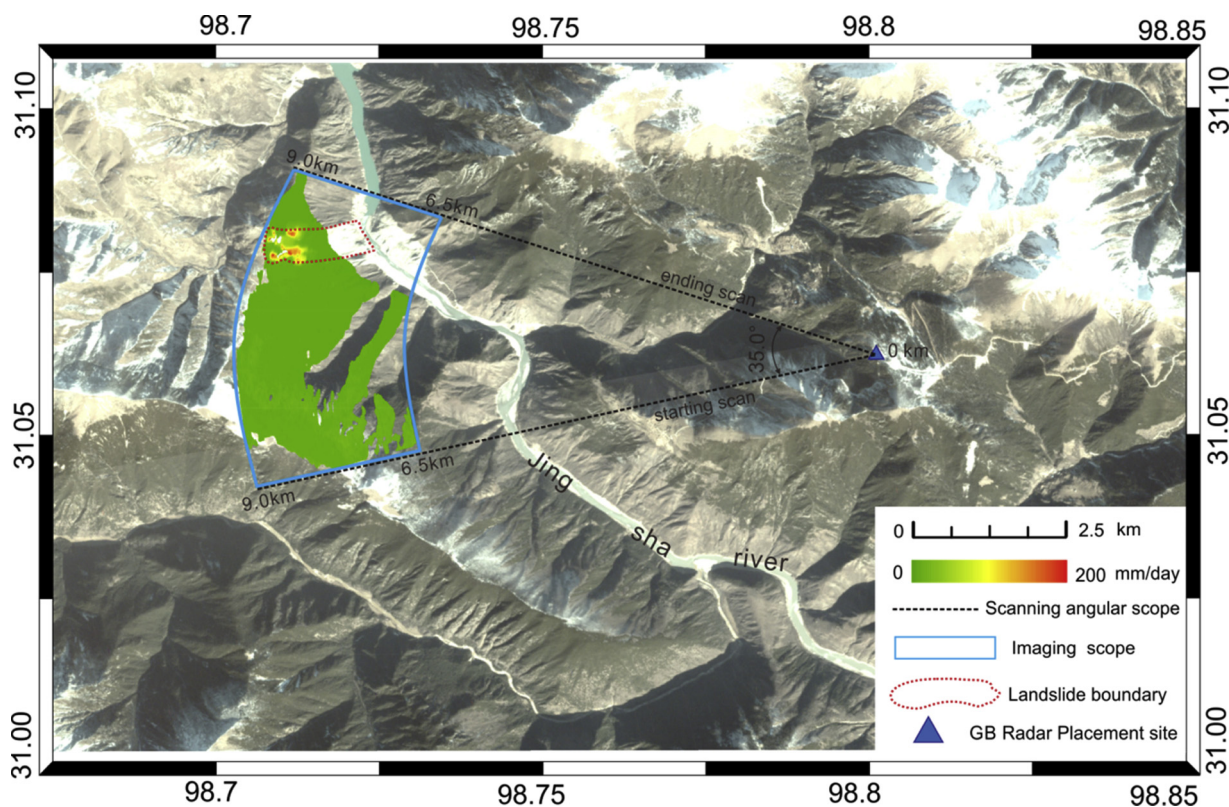

Fig. 4. Geocoded results of the mean velocity map. The base map is based on planet satellite imagery with a resolution of 3 m and was acquired on Dec. 7 2018. The colour version of this figure is available only in the online version.

points decreased, which also indicates that these marginal fracture areas are gradually becoming stable.

3.2. Space-borne SAR pixel-offset tracking (POT)

We collected an ascending track of COSMO-SkyMed SAR data with 3 m resolution acquired on Nov. 30 and Dec. 11, 2018. Gamma Software was used (Werner et al., 2010) to process the entire procedure of the pixel offset tracking. The average slip rate of the landslide in Fig. 8 shows that there is a phenomenon similar to interferometry de-coherence in certain areas of the landslide surface. This phenomenon

occurs largely due to the surface weathered debris and sand. The signal characteristics of these areas on the SAR images change over time, so these points will be excluded during offset tracking processing. In the azimuth offset displacement fields, the positive and negative values represent displacement along and opposite to the satellite flight direction, respectively. A maximum deformation rate of -350 mm/day along the azimuth direction is identified (Fig. 8A). There are many negative value dots on the left side of the sliding bed (assuming our line of sight is in the direction of radar signal propagation), which represent the opposite direction of the satellite orbit. The negative value dots indicate that the left landslide body moves toward the middle
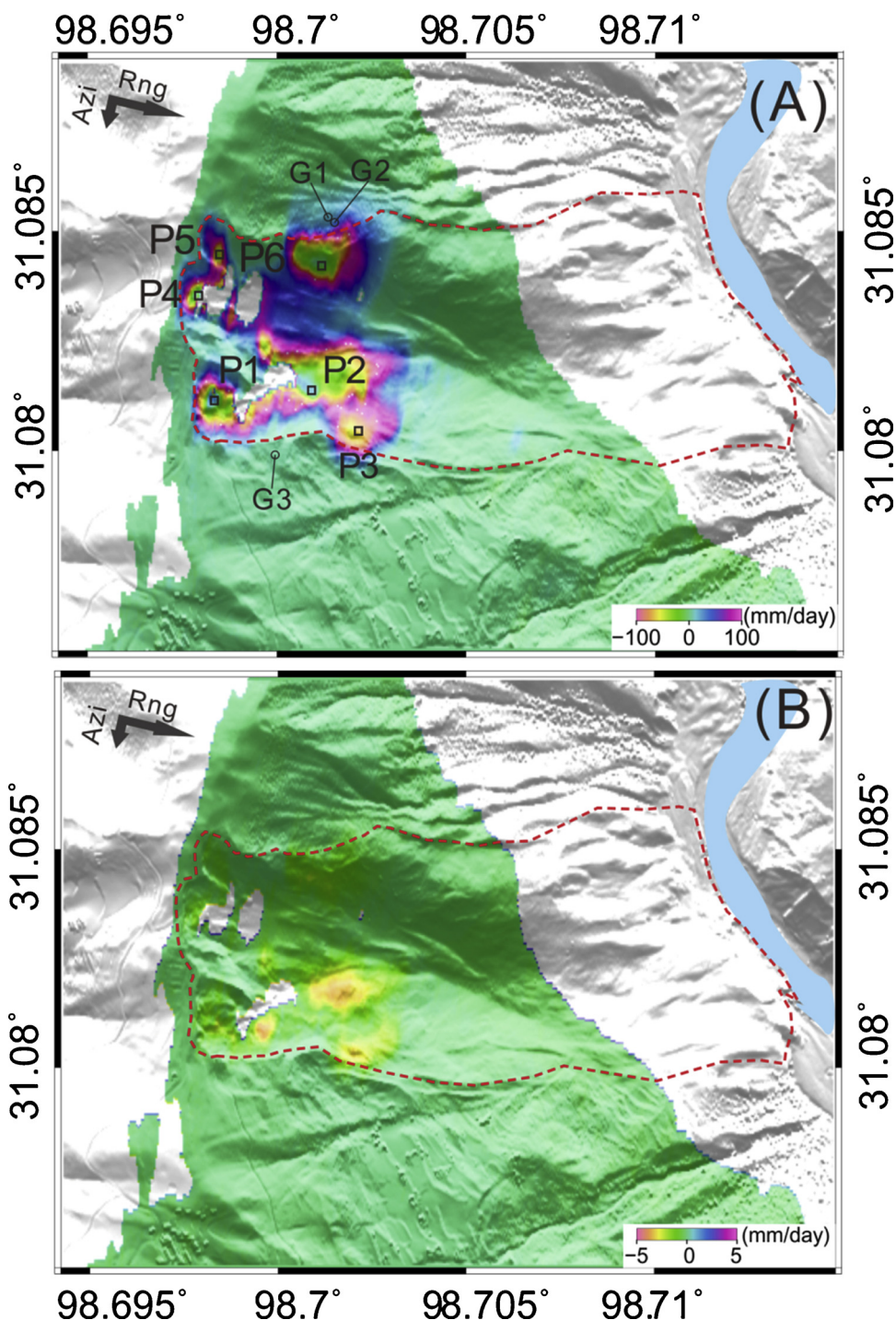
Fig. 5. (A) Enlarged mean velocity map from the stacked interferograms. The polygon delineated by red dotted lines indicates the main deformation region Six points (P1-P6) were selected for the time series in Fig. 6. (B) The residual results of InSAR stacking. The colour version of this figure is available only in the online version.

(southward), while the dots with positive values on the right side of the landslide indicate that the landslide body in these positions moves toward the center of the landslide bed. In the range offset displacement map (Fig. 8B), the positive and negative values represent displacement away from and toward the satellite, respectively. A maximum deformation rate of 400 mm/day along the range direction is identified. Because the signal propagation direction of the satellite is consistent with the movement direction of the landslide body, the deformation field mainly moves away from the satellite. The westward movement points are not very obvious, which corresponded with the results of the GBR, indicating that the deformation in these areas is mainly moving

toward the river.

3.3. Three-dimensional results

In this study, the antenna incidence angle of GBR was set to 5 degrees below horizontal and the radar signal can be considered to propagate nearly parallel to the surface. Therefore, the radar signal is sensitive to horizontal deformation, but the displacements perpendicular to the LOS direction are missed (Bardi et al., 2014). This phenomenon is one of the limitations of the GBR technique, and thus, by combining satellite and ground-based SAR observations, we can obtain
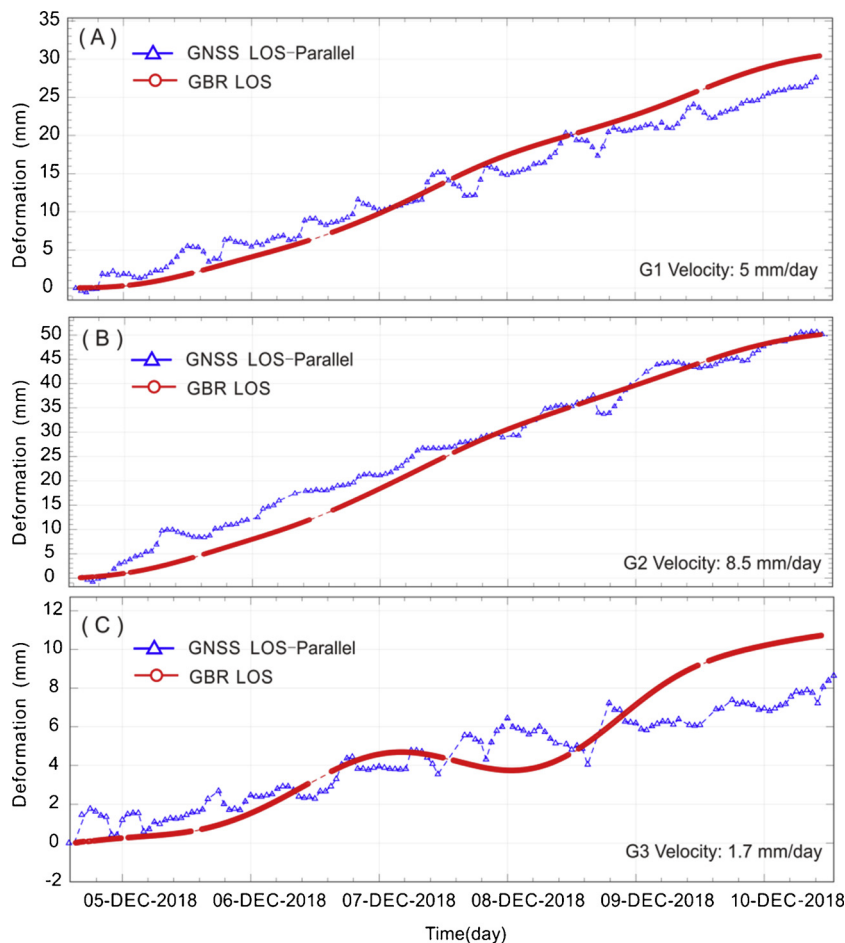
Fig. 6. Comparisons of deformation results between GBR LOS and GNSS LOS-parallel directions.

a 3D deformation result (Corsini et al., 2006; Bardi et al., 2014; Frodella et al., 2016; Carlà et al., 2018; Wang et al., 2018b,c).

According the method presented in Section 2.4, we obtain the results of the quasi-3D deformation fields (Fig. 9), which show that the obvious deformation characteristics in the three-dimensional deformation field correspond to the region with large deformation regions in Fig. 5A. Because the deformation is too small to be measurable using the POT technique in the trailing edge area (Fig. 8), 3D deformation results are mainly concentrated on the landslide surface. The position and direction of the arrows indicate that the deformation is mainly distributed on the sliding bed and the boundary of the trailing edge and sliding bed. The moving rock mass converges to the center of the sliding bed, which is consistent with the 3D landslide landform in Fig. S1. The

residual rock and debris at the posterior margin of the sliding bed converge to the middle and then move downward to the river.

4. Discussion

4.1. Stability analysis of the landslide body

The results of the ground-based and space-borne radar observations show that the main deformation occurred in the weathered area above the bedrock and that there is no obvious deformation below the bedrock line of the landslide, which is presented in Figs. 8 and 9. The results in Fig. 9 show that the spatial distribution of the deformation is heterogeneous. Very large deformation only appeared in certain local
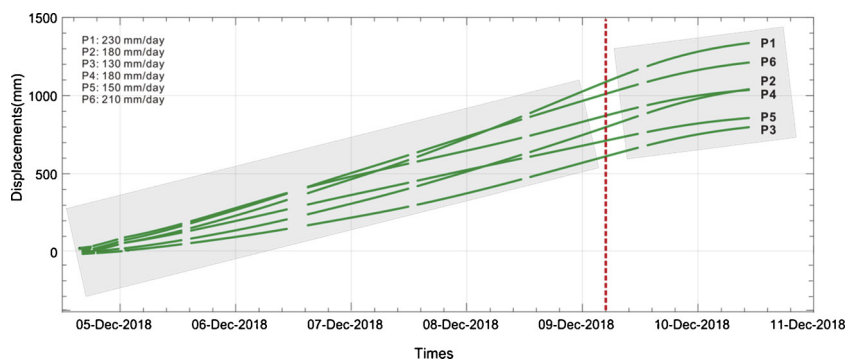

Fig. 7. Cumulative deformation of six selected points during the 6-day survey. The red dotted line represents the demarcation line of deformation rate change in time, and the gray rectangles indicate the overall deformation rate trends for two time periods. The colour version of this figure is available only in the online version.
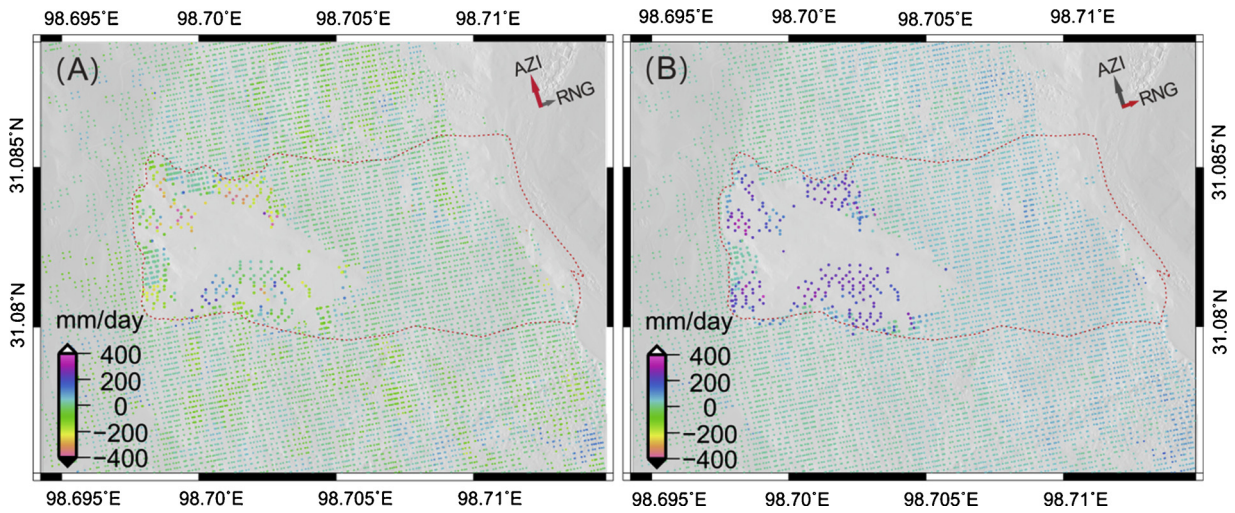
Fig. 8. Pixel-offset tracking results of SAR images. (A) Azimuth direction deformation and (B) range direction deformation. The colour version of this figure is available only in the online version.

areas, which indicates that the overall landslide is in a relatively and transitorily stable state. According to the shape of the slide bed and the material of the surface, the landslide can be divided into highly weathered areas, weakly weathered areas, and bedrock areas (Fig. 10). The findings show that the bedrock is very stable and that there is no new separated block. The weathered materials above the bedrock line are loose and easily deformable, and are supported and stabilized by the lower bedrock. Currently, large landslides will not form because there are no new separated blocks in the lower part. Both the highly and weakly weathered areas were filled with looser and weaker rock mass, which lacks cohesive strength and can be considered more easily collapsed than bedrock. The area below the bedrock line is composed of slightly weathered or fresh rock. The deformation results noted above show that there is no obvious displacement in this area. Therefore, the bedrock below the landslide body is stable. As shown in Fig. 10, Joint 1

and Joint 2 in the bedrock had formed a sliding aisle before the landslides occurred. The existence of the two joints could be considered as one of the root causes of these landslides. Another root cause is the weak strength of the weathered areas above the bedrock, as discussed above. Currently, the upper landslide bodies have slid into the Jinsha River, and no new sliding aisle or new dangerous joints were found from the current optical image data. The weathered rock mass above the bedrock line is relatively stable based on the strong supports of the bedrock, except for certain partly small-scale partial collapses.

Since the second Baige landslide event on Nov. 3, 2018, the landslide remnants have been in constant adjustment and deformation. These changes have mainly manifested as small collapses and the accumulation of loose deposits in the landslide trough. Due to the smaller thickness of the deposits (1–3 meters), there is little possibility of large-scale sliding, and there is a small possibility of the river being blocked
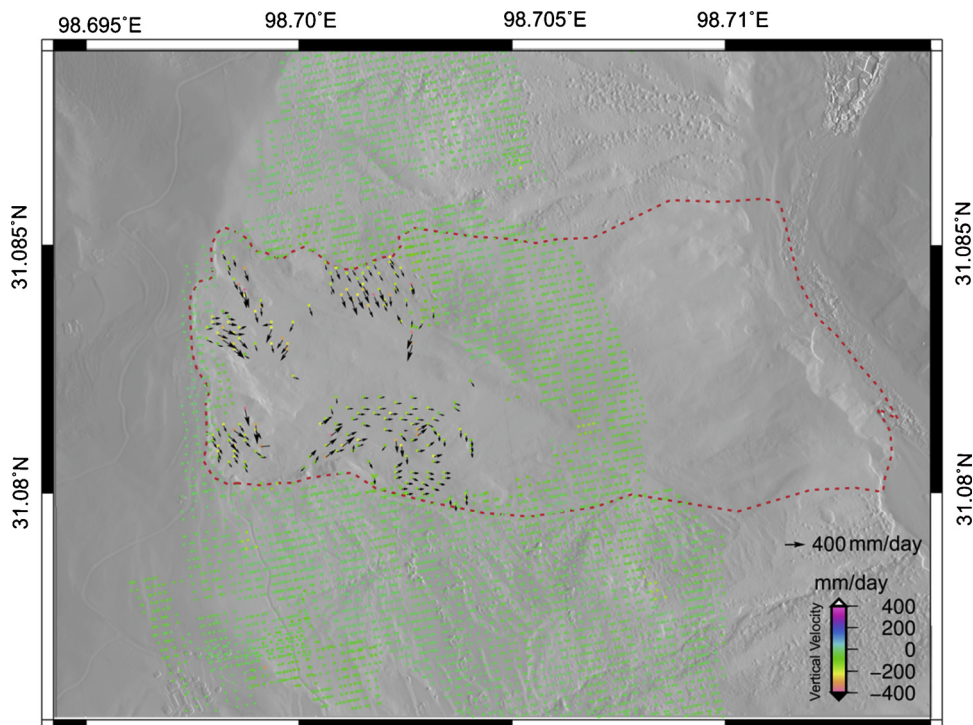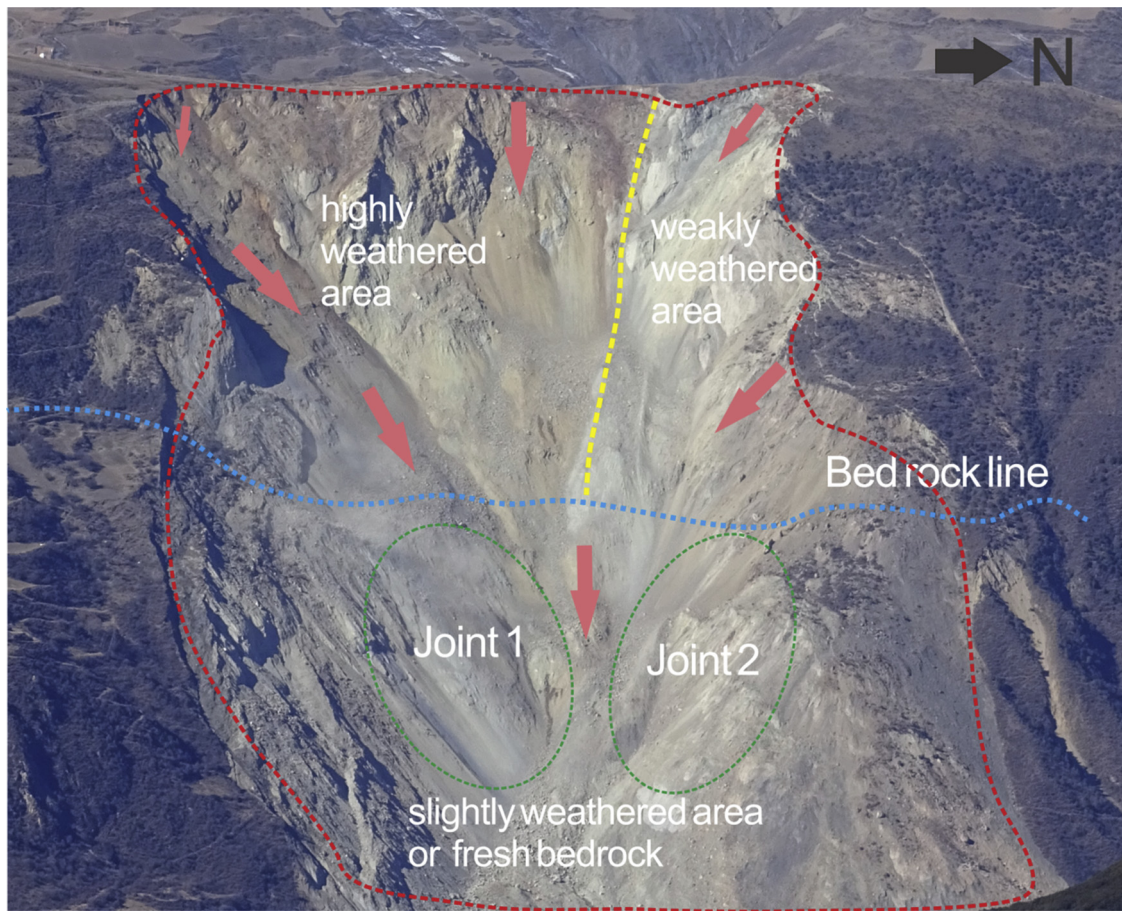

Fig. 9. Quasi-3D displacement fields using space-borne and ground-based observations. The colour version of this figure is available only in the online version.

Fig. 10. Partitioning and stability analysis of the landslide body from close-range photography. The red arrows indicate the direction of landslide movement interpreted from the 3D deformation fields. The colour version of this figure is available only in the online version.

by sliding alone. Some of the rock and debris may enter the river, but there will be no long-term narrowing of the river and no significant change in the flow capacity of the river.

4.2. Distributed and deformation characteristics of trailing edge cracks

After the Baige landslides, a high and steep slope is newly formed on the back wall and left and right sides of the landslide trough. The stress adjustment of the new slope is still in progress. The second landslide on November 3, 2018, was the result of this adjustment. At present, the slope has not reached a stable state, which is also confirmed by the existence of a large number of cracks in the back edge and left and right slopes of the landslide (Fig. 11).

We selected six of the remaining available GNSS devices for deformation time series analysis (white rectangular points in Fig. 11). The time period we selected ranged from Dec. 2 to Dec. 12, which covers the time period of ground-based radar monitoring in this paper. Two deformation components with horizontal and vertical orientations were employed to identify the stability of the trailing edges, and a 1-day sampling interval was used. Taking Dec. 2, 2018 as the reference time, we analyzed the cumulative deformation of horizontal and vertical deformation (Fig. 12). The results show that the horizontal deformation is obviously larger than the vertical deformation. The maximum deformation rate of G2 is up to 12 mm/day horizontally and 6 mm/day vertically. On the right and back side of the trailing edge, the deformation is relatively small, only 1–3 mm/day (see G3 in Figs. 11 and 12).

After the occurrence of the two large-scale landslides, some weathered rock and debris still exist in the source area. More attention

should be paid to the trailing edge of the landslide, especially on the left side, although the volume of the rock mass is not as large as in the previous two events. The scale of the cracks will directly determine the stability of the slope, which impacts on upstream and downstream reaches. If these cracks collapse at the same time, the rock and soil entering the river may cause river narrowing. These impacts will not be obvious if the adjustment is accomplished by long-term and small-scale landslides.

4.3. Risk of landslides in the future

Landslides are caused by instability of rock and soil under many internal and external dynamic actions. There are a large number of remnants around the sliding trough that have lost support or are under traction due to the landslide. These remnants have been cut by a large number of cracks and separated from the parent slope. Their stability is poor, and the remnants landslides will inevitably occur again with different scales. Slope movement occurs when the force applied on the slope (mainly due to gravity) exceeds the strength of the rock. Two main factors may trigger the gravity force effects on the trailing edge of the Baige Landslide.

(1) Seismic activity. In steep topographic relief and landslide-prone areas, earthquakes greatly increase the likelihood of landslides and have been inferred as one of the main predisposing factors of frequent landslide disasters (Li et al., 2019). Several large earthquakes have occurred near the location of these two landslides within 125 km range, such as the 1842 Zongguo earthquake (Mw 7.3), 1870 Batang earthquake (Mw 7.2) and 1989 earthquake (Mw 6.5),
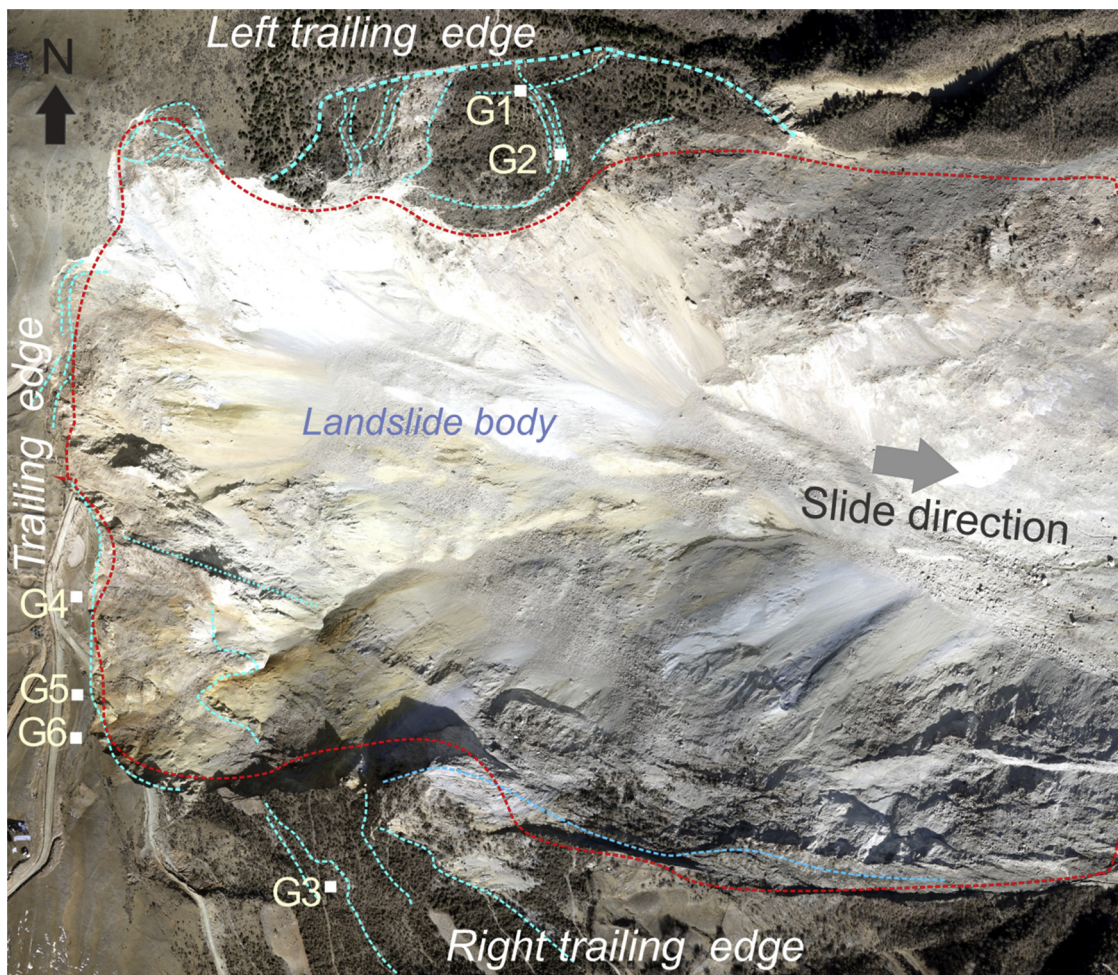
Fig. 11. Orthophoto map acquired from the UAV platform on Dec. 6, 2018. The blue dotted lines in the picture are interpreted as landslide cracks. The white rectangular points represent the location of GNSS satellite displacement monitoring sites. The red polygon represents the landslide body region. The colour version of this figure is available only in the online version.

but no earthquakes larger than Mw 6.0 were reported in the past 100 years within 50 km (Fan et al., 2019). Two earthquakes occurred more than 100 km away from the landslide site on Dec. 13, 2018, and Jan. 5, 2019. The magnitudes of these earthquakes were Ms 4.9 and Ms 3.1, respectively. The GNSS observation results show that two small earthquakes have little effect on the landslide state unless an earthquake of moderate or high intensity occurs in the area (supporting information Fig. S2).

(2) Water. The immersion of the slope in water is another main factor

that may lead to landslides. This effect may be caused by heavy rainfall, snow melt, and changes in the groundwater level. Starting in May of each year, the region enters the rainy season and ice and snow begin to melt. Therefore, the precipitation gradually increases and the stability of landslides during this period requires additional monitoring.
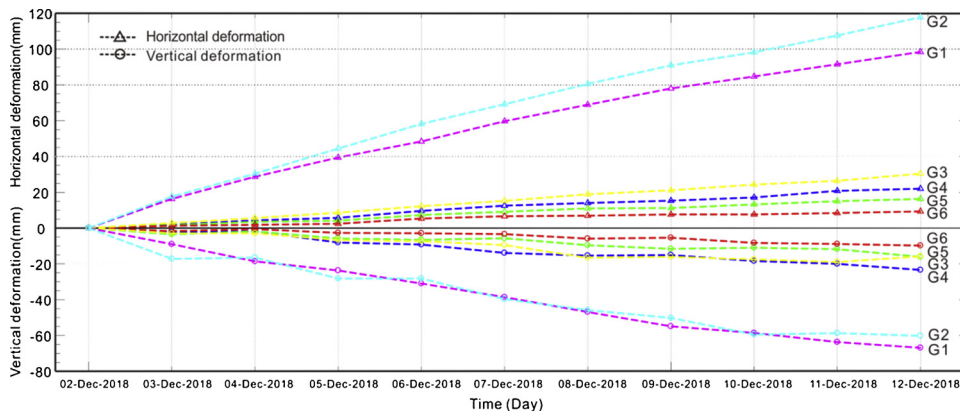

Fig. 12. Cumulative deformation of six GNSS measurements in trailing edge regions. Each measurement includes two components: horizontal and vertical.

4.4. Improvement scheme of GBR measurements

In this paper, ground-based SAR is used to monitor the near real-time deformation of landslides. Comparing the results from ground-based radar and POT, it can be seen that the maximum deformation rate of ground-based radar is smaller than that of POT. This difference mainly arises because there are many obvious incoherent areas in ground-based radar results, which are relatively large deformation areas that exceed the deformation gradient limits of GBR, resulting in the void of the deformation field. Therefore, we summarized the characteristics of GBR devices and the particularity of this landslide and propose the following improvement scheme for future ground-based radar monitoring of similar landslide circumstances.

(1) Increasing sampling frequency. A 10-minute sampling interval is used in this paper. There are still obvious decoherence and atmospheric error effects in the interferogram. To suppress the effects of decoherence and atmospheric errors, the data acquisition frequency should be increased, for example, once every 5 min.
(2) Close-range observation. Because of the limitation of the geographical location of landslides in this study, the GBR is deployed at a distance of 8 km, causing several insurmountable observational constraints, e.g., low resolution and atmospheric environmental change. Therefore, it is necessary to increase the close-range observation in the future measurement work.
(3) Multi-angle measurement. Due to the influence of single observation angle, it is impossible to fully characterize the deformation characteristics. Multi-angle surveys could avoid topographic shadowing effects and maximize displacement signals in the slope-parallel direction.

5. Conclusion

Based on ground-based radar deformation observations from Dec. 4 to Dec. 10, 2018, and space-borne SAR data pixel offset tracking, the deformation characteristics of residual rocks and debris in the sliding bed after two Baige landslide events in 2018 were analyzed. To better identify the boundary and deformation distribution of the unstable areas, the comprehensive results derived from ground-based and space-borne radar sensors revealed that the sliding bed is currently in a relatively stable state except some residual rock masses and debris. However, there are many obvious cracks in the trailing edge of the landslide, which are still in a constant state of deformation. Although their moving rate is much smaller than that of the residual rock mass and debris on the sliding bed, their volume is relatively large enough to narrow the river. Therefore, the stability of these areas needs to be closely monitored, especially during the rainy season.

By characterizing the deformation of landslides in real time, the relationship between the information and the evolution stage of landslide disasters can be mapped. SAR/InSAR technology can be used to obtain the surface deformation of the landslide body and to characterize the sliding scale, active stage and development trend of the landslide mass. To compensate for the inadequate observation capability of the space-borne SAR/InSAR system (observation direction and continuous monitoring), the recent combined application of ground-based SAR and space-borne SAR/InSAR has been important for early identification of new landslides, long-term monitoring of old landslides and stability evaluation after large landslides.

Acknowledgments

Appendix A. Supplementary data

Supplementary material related to this article can be found, in the online version, at doi:https://doi.org/10.1016/j.jag.2019.101949.

References

Atkins, C., Ziebart, M., 2016. Effectiveness of observation-domain sidereal filtering for GPS precise point positioning. GPS Sol. 20, 111–122. https://doi.org/10.1007/s10291-015-0473-1.

Bardi, F., Frodella, W., Ciampalini, A., Bianchini, S., Del Ventisette, C., Gigli, G., Fanti, R., Moretti, S., Basile, G., Casagli, N., 2014. Integration between ground based and satellite SAR data in landslide mapping: the San Fratello case study. Geomorphology 223, 45–60. https://doi.org/10.1016/j.geomorph.2014.06.025.

Berardino, P., Fornaro, G., Lanari, R., Sansosti, E., 2002. A new algorithm for surface deformation monitoring based on small baseline differential SAR interferograms. IEEE Trans. Geosci. Remote Sens. 40 (11), 2375–2383. https://doi.org/10.1109/TGRS.2002.803792.

Bozzano, F., Cipriani, I., Mazzanti, P., Prestininzi, A., 2011. Displacement patterns of a landslide affected by human activities: insights from ground-based InSAR monitoring. Nat. Hazards 59 (3), 1377–1396. https://doi.org/10.1007/s11069-011-9840-6.

Caduff, R., Schlunegger, F., Kos, A., Wiesmann, A., 2015. A review of terrestrial radar interferometry for measuring surface change in the geosciences. Earth Surf. Process. Landf. 40 (2), 208–228. https://doi.org/10.1002/esp.3656.

Caduff, R., Wiesmann, Andreas, Bühler, Yves, Bieler, Claudia, Limpach, Philippe, 2016. Terrestrial radar interferometry for snow glide activity monitoring and its potential as precursor of wet snow avalanches. 13th Congress Interpraevent 2016: Living With Natural Risks, Lucerne, Switzerland. Conference Proceedings. pp. 239–248.

Calabro, M.D., Schmidt, D.A., Roering, J.J., 2010. An examination of seasonal deformation at the Portuguese Bend landslide, southern California, using radar interferometry. J. Geophys. Res. 115 (F2). https://doi.org/10.1029/2009jf001314.

Carlà, T., Farina, P., Intrieri, E., Ketizmen, H., Casagli, N., 2018. Integration of ground-based radar and satellite InSAR data for the analysis of an unexpected slope failure in an open-pit mine. Eng. Geol. 235, 39–52. https://doi.org/10.1016/j.enggeo.2018.01.021.

Casagli, N., Catani, F., Del Ventisette, C., 2010a. Monitoring, prediction, and early warning using ground-based radar interferometry. Landslides 7 (3), 291–301. https://doi.org/10.1007/s10346-010-0215-y.

Casagli, N., Luzi, G., Del Ventisette, C., 2010b. Monitoring deformations of the Sciara del Fuoco (Stromboli) through ground-based radar interferometry. Acta vulcanologica 22 (1/2), 77–84.

Corsini, A., Farina, P., Antonello, G., Barbieri, M., Casagli, N., Coren, F., Tarchi, D., 2006. Space-borne and ground-based SAR interferometry as tools for landslide hazard management in civil protection. Int. J. Remote Sens. 27 (12), 2351–2369. https://doi.org/10.1080/01431160600554405.

Chen, C.W., Zebker, H.A., 2002. Phase unwrapping for large SAR interferograms: statistical segmentation and generalized network models. IEEE Trans. Geosci. Remote Sens. 40 (8), 1709–1719. https://doi.org/10.1109/TGRS.2002.802453.

Dai, K., Li, Z., Tomás, R., Liu, G., Yu, B., Wang, X., Cheng, H., Chen, J., Stockamp, J., 2016. Monitoring activity at the Daguangbao mega-landslide (China) using Sentinel-1 TOPS time series interferometry. Remote Sens. Environ. 186, 501–513. https://doi.org/10.1016/j.rse.2016.09.009.

Deng, J., Gao, Y., Yu, Z., Xie, H., 2019. Analysis on the formation mechanism and process of Baige Landslides damming the upper reach of Jinsha River (In Chinese), China. Adv. Eng. Sci. 51 (1), 9–16. https://doi.org/10.15961/j.jsuese.201801438.

Fan, X., Xu, Q., Alonso-Rodriguez, A., Subramanian, S.S., Li, W., Zheng, G., Dong, X., Huang, R., 2019. Successive landsliding and damming of the Jinsha River in eastern Tibet, China: prime investigation, early warning, and emergency response. Landslides. 16, 1003–1020. https://doi.org/10.1007/s10346-019-01159-x.

Fielding, E.J., Lundgren, P.R., Taymaz, T., Yolsal-Çevikbilen, S., Owen, S.E., 2013. Fault-slip source models for the 2011 M 7.1 Van earthquake in Turkey from SAR interferometry, pixel offset tracking, GPS, and seismic waveform analysis. Seismol. Res. Lett. 84 (4), 579–593. https://doi.org/10.1785/0220120164.

Frodella, W., Ciampalini, A., Gigli, G., Lombardi, L., Raspini, F., Nocentini, M., Scardigli, C., Casagli, N., 2016. Synergic use of satellite and ground based remote sensing methods for monitoring the San Leo rock cliff (Northern Italy). Geomorphology 264, 80–94. https://doi.org/10.1016/j.geomorph.2016.04.008.

Goldstein, R.M., Werner, C.L., 1998. Radar interferogram filtering for geophysical applications. Geophys. Res. Lett. 25 (21), 4035–4038. https://doi.org/10.1029/1998GL900033.

Handwerger, A.L., Huang, M.H., Fielding, E.J., Booth, A.M., Bürgmann, R., 2019. A shift from drought to extreme rainfall drives a stable landslide to catastrophic failure. Sci. Rep. 9 (1), 1569. https://doi.org/10.1038/s41598-018-38300-0.

Herrera, G., Fernendez-Merodo, J.A., Mulas, J., Pastor, M., Luzi, G., Monserrat, O., 2009. A landslide forecasting model using ground based sar data: the portalet case study. Eng. Geol. 105 (3-4), 220–230. https://doi.org/10.1016/j.enggeo.2009.02.009.

Highland, L.M., Bobrowsky, P., 2008. The landslide handbook-a guide to understanding landslides. U.S. Geol. Surv. Circ. 1325, 129.

Himematsu, Y., Furuya, M., 2016. Fault source model for the 2016 Kumamoto earthquake sequence based on ALOS-2/PALSAR-2 pixel-offset data: evidence for dynamic slip partitioning. Earth Planets Space 68, 169. https://doi.org/10.1186/s40623-016-0545-7.

Hu, X., Wang, T., Pierson, T.C., Lu, Z., Kim, J., Cecere, T.H., 2016. Detecting seasonal landslide movement within the Cascade landslide complex (Washington) using time-series SAR imagery. Remote Sens. Environ. 187, 49–61. https://doi.org/10.1016/j.rse.2016.10.006.

Hu, X., Lu, Z., Pierson, T.C., Kramer, R., George, D.L., 2018. Combining InSAR and GPS to determine transient movement and thickness of a seasonally active low-gradient translational landslide. Geophys. Res. Lett. 45, 1453–1462. https://doi.org/10.1002/2017GL076623.

Li, W., Chen, Y., Liu, F., Yang, H., Liu, J., Fu, B., 2019. Chain-style landslide hazardous process: constraints from seismic signals analysis of the 2017 Xinmo landslide, SW China. J. Geophys. Res. Solid Earth 124. https://doi.org/10.1029/2018JB016433.

Lowry, B., Gomez, F., Zhou, W., Mooney, M.A., Held, B., Grasmick, J., 2013. High resolution displacement monitoring of a slow velocity landslide using ground based radar interferometry. Eng. Geol. 166, 160–169. https://doi.org/10.1016/j.enggeo.2013.07.007.

Luzi, G., Pieraccini, M., Mecatti, D., Noferini, L., Macaluso, G., Galgaro, A., Atzeni, C., 2006. Advances in ground-based microwave interferometry for landslide survey: a case study. Int. J. Remote Sens. 27 (12), 2331–2350. https://doi.org/10.1080/01431160600554975.

Luzi, G., Pieraccini, M., Mecatti, D., Noferini, L., Macaluso, G., Tamburini, A., Atzeni, C., 2007. Monitoring of an alpine glacier by means of ground-based SAR interferometry. IEEE Geosci. Remote Sens. Lett. 4 (3), 495–499. https://doi.org/10.1109/LGRS.2007.898282.

Monserrat, O., Crosetto, M., Luzi, G., 2014. A review of ground-based SAR interferometry for deformation measurement. ISPRS-J. Photogramm Remote Sens. 93, 40–48. https://doi.org/10.1016/j.isprsjprs.2014.04.001.

Noferini, L., Mecatti, D., Macaluso, G., Pieraccini, M., Atzeni, C., 2009. Monitoring of Belvedere Glacier using a wide angle GB-SAR interferometer. J. Appl. Geophys. 68 (2), 289–293. https://doi.org/10.1016/j.jappgeo.2009.02.004.

Pierson, T.C., Lu, Z., 2009. InSAR detection of renewed movement of a large ancient landslide in the Columbia River Gorge, Washington. Geological Society of America Abstract With Programs, 2009 Portland Annual Meeting 41 (7), 497.

Raucoules, D., De Michele, M., Malet, J.P., Ulrich, P., 2013. Time-variable 3D ground displacements from high-resolution synthetic aperture radar (SAR). Application to La Valette landslide (South French Alps). Remote Sens. Environ. 139, 198–204. https://doi.org/10.1016/j.rse.2013.08.006.

Rouyet, L., Kristensen, L., Derron, M.H., Michoud, C., Blikra, L.H., Jaboyedoff, M., Lauknes, T.R., 2017. Evidence of rock slope breathing using ground-based InSAR. Geomorphology 289, 152–169. https://doi.org/10.1016/j.geomorph.2016.07.005.

Serrano-Juan, A., Vázquez-Sunè, E., Monserrat, O., Crosetto, M., Hoffmann, C., Ledesma, A., Criollo, R., Pujades, E., Velasco, V., Garcia-Gil, A., Alcarze, M., 2016. Gb-sar interferometry displacement measurements during dewatering in construction works case of la sagrera railway station in barcelona, spain. Eng. Geol. 205 (29), 104–115. https://doi.org/10.1016/j.enggeo.2016.02.014.

Sun, Q., Zhang, L., Ding, X.L., Hu, J., Li, Z.W., Zhu, J.J., 2015. Slope deformation prior to Zhouqu, China landslide from InSAR time series analysis. Remote Sens.Environ. 156, 45–57. https://doi.org/10.1016/j.rse.2014.09.029.

Tapete, D., Casagli, N., Luzi, G., Fanti, R., Gigli, G., Leva, D., 2013. Integrating radar and laser-based remote sensing techniques for monitoring structural deformation of archaeological monuments. J. Arch. Sci. 40 (1), 176–189. https://doi.org/10.1016/j.jas.2012.07.024.

Tarchi, D., Casagli, N., Moretti, S., et al., 2003. Monitoring landslide displacements by using ground-based synthetic aperture radar interferometry: application to the Ruinon landslide in the Italian. Alps. J. Geophys. Res 108 (B8-2387), 101–114. https://doi.org/10.1029/2002jb002204.

Tong, X., Schmidt, D., 2016. Active movement of the cascade landslide complex in Washington from a coherence-based insar time series method. Remote Sens. Environ. 186, 405–415. https://doi.org/10.1016/j.rse.2016.09.008.

Wang, T., Jónsson, S., 2015. Improved SAR amplitude image offset measurements for deriving three-dimensional coseismic displacements. IEEE J. Sel. Top. Appl. Earth Observ. Remote Sens. 8 (7), 3271–3278. https://doi.org/10.1109/JSTARS.2014.2387865.

Wang, T., Shi, Q., Nikkhoo, M., Wei, S., Barbot, S., Dreger, D., Bürgmann, R., Motagh, M., Chen, Q.F., 2018a. The rise, collapse, and compaction of Mt. Mantap from the 3 September 2017 North Korean nuclear test. Science 361 (6398), 166–170. https://doi.org/10.1126/science.aar7230.

Wang, Z., Li, Z., Mills, J., 2018b. A new approach to selecting coherent pixels for ground-based SAR deformation monitoring. ISPRS-J. Photogr. Remote Sens. 144, 412–422. https://doi.org/10.1016/j.isprsjprs.2018.08.008.

Wang, Z.W., Yu, S., Tao, Q., Liu, G., Hao, H., Wang, K., Zhou, C., 2018c. A method of monitoring three-dimensional ground displacement in mining areas by integrating multiple InSAR methods. Int. J. Remote Sens. 39, 1199–1219. https://doi.org/10.1080/01431161.2017.1399473.

Werner, C., Wegmüller, U., Strozzi, T., Wiesmann, A., 2010. Gamma SAR and interferometric processing software. Proceedings of the Ers-Envisat Symposium, Gothenburg, Sweden Vol. 1620 p. 1620.

Xie, S., Dixon, T.H., Voytenko, D., Deng, F., Holland, D.M., 2018. Grounding line migration through the calving season at Jakobshavn Isbræ, Greenland, observed with terrestrial radar interferometry. Cryosphere 12 (4), 1–29. https://doi.org/10.5194/tc-12-1387-2018.

Xu, Q., Zheng, G., Li, W., He, C., Dong, X., Guo, C., Feng, W., 2018. Study on successive landslide damming events of Jinsha River in Baige Village on Octorber 11 and Novermber 3, 2018. J. Eng. Geol. 26 (6), 1534–1551. https://doi.org/10.13544/j.cnki.jeg.2018-406. [in Chinese].

Zebker, H.A., Rosen, P.A., Hensley, S., 1997. Atmospheric effects in interferometric synthetic aperture radar surface deformation and topographic maps. J. Geophys. Res. Solid Earth 102 (B4), 7547–7563. https://doi.org/10.1029/96jb03804.